Oxidation of nanoscale Au–In alloy particles as a possible route toward stable Au-based catalysts

Eli A. Sutter[1], Xiao Tong, Katherine Jungjohann, and Peter W. Sutter

Center for Functional Nanomaterials, Brookhaven National Laboratory, Upton, NY 11973

Edited by Gabor A. Somorjai, University of California, Berkeley, CA, and approved May 9, 2013 (received for review March 20, 2013)

The oxidation of bimetallic alloy nanoparticles comprising a noble and a nonnoble metal is expected to cause the formation of a single-component surface oxide of the nonnoble metal, surrounding a core enriched with the noble metal. Studying the room temperature oxidation of Au–In nanoparticles, we show that this simple picture does not apply to an important class of bimetallic alloys, in which the oxidation proceeds via predominant oxygen diffusion. Instead of a crystalline In_2O_3 shell, such oxidation leads to an amorphous shell of mixed Au–In oxide that remains stable to high temperatures and whose surface layer is enriched with Au. The Au-rich mixed oxide is capable of adsorbing both CO and O_2 and converting them to CO_2, which desorbs near room temperature. The oxidation of Au–In alloys to a mixed Au–In oxide shows significant promise as a viable approach toward Au-based oxidation catalysts, which do not require any complex synthesis processes and resist deactivation up to at least 300 °C.

transmission electron microscopy | temperature programmed desorption | X-ray photoelectron spectroscopy

The importance of metal nanoparticles for a wide variety of applications, e.g., in catalysis, sensing, etc., has sparked interest in understanding and controlling their oxidation. The formation of an oxide layer negatively affects performance in applications that require pure metal surfaces. However, oxidation can be advantageous as it opens a way for engineering complex structures. Our understanding of room temperature oxidation has been established primarily in studies on the oxidation of bulk materials or planar films (1). Most of this insight should apply directly to the oxidation of nanoparticles, but important aspects arise in the geometry of small particles. For example, the high curvature in a nanoparticle can drive oxidation to larger thicknesses than in the planar case (2–4). Nanoscale junctions and interfaces to other materials can promote enhanced oxidation, as well as the formation of well-ordered epitaxial oxide segments (5). The oxidation of nanoparticles is also a powerful mechanism to produce nanoscale heterostructures. Metals that oxidize via predominant anion diffusion [In (2, 5), Pb (6), Sn, among others] form metal-oxide core–shell nanoparticles. For metals that oxidize via fast cation diffusion [Co (7), Al (6), Fe (8), Ni (9), among others], nanoscale porosity buildup creates hollow oxide nanocrystals that can be used as cages, e.g., to be filled with different materials (7) for storage or protection.

Bimetallic (alloy, core–shell, etc.) nanoparticles promise widely tunable properties, and much progress has recently been made in their controlled synthesis (10). The oxidation of bimetallic nanoparticles has been studied much less than that of elemental metals, but it could provide even more interesting opportunities for the fabrication of functional nanomaterials, for example in catalysis.

Alloys that comprise a noble and a less noble metal component are of interest because their oxidation can give rise to a variety of catalytically active configurations, such as oxide-supported noble metal nanoparticles, core–shell structures, etc. A noble metal that has attracted particular interest is gold. Bulk Au is inert and is the only transition metal that is not catalytically active, except in very isolated cases (11, 12). The inability of bulk Au surfaces to activate O_2 is the main factor limiting their activity as an oxidation catalyst. However, Au can become an exceptionally active low-temperature oxidation catalyst if it can be supplied with atomic oxygen, e.g., Au nanoparticles on reducible metal oxide supports (13, 14), Au nanoparticles on nonreducible oxides, where O_2 activation can be achieved by the activation of other small molecules (e.g., H_2) and generation of an O-containing intermediate (15), Au with chemisorbed oxygen (16), and surface or bulk Au oxides (17). Although the activity of carefully prepared Au CO oxidation catalysts is unmatched by other metals, Au nanoparticle catalysts face limitations due to their complex synthesis and their propensity for sintering. Similarly, Au surfaces with chemisorbed oxygen require specialized preparations suitable only for model catalyst studies (e.g., by oxygen sputtering or exposure to ozone) and readily deactivate, especially at elevated temperatures.

Previous studies have shown that the oxidation of binary alloys between Au and a less noble metal (M) produces either Au/M-oxide particle aggregates or core–shell structures with Au core and M-oxide shell. Early work by Koeppel et al. (18), for example, showed that the oxidation of amorphous $Au_{25}Zr_{75}$ produces Au nanoparticles on ZrO_2, which are active in CO_2 hydrogenation. Similarly, the oxidation of an Au–Ni alloy leads to the formation of coupled Au–NiO aggregates in the form of Au particles connected to NiO particles; on SiO_2 support these heterostructures showed enhanced activity in low-temperature CO oxidation (19, 20). Both Au–Cu (21–23) and Au–Sn (24) alloy nanoparticles are transformed to core–shell structures upon oxidation, consisting of Au cores and CuO_x or SnO_2 shells, respectively. Supported on SiO_2, these heterostructures showed higher CO oxidation activity than metallic Au–Cu alloy particles or nonencapsulated Au particles on SnO_2. The enhancement in activity due to oxidation appears to be support specific, and metallic Au-Cu, for instance, was found to be an active oxidation catalyst on reducible oxides (25).

Here, we study the room temperature oxidation of binary alloys that comprise Au and a less noble metal component and whose oxidation is dominated by anion diffusion. These systems differ from those considered previously in that they neither produce nanoparticle aggregates nor involve a phase separation to a core–shell structure of an Au core encapsulated in an oxide of the less noble metal at the surface. We focus on the room temperature oxidation of Au–In alloy nanoparticles with two different compositions. The oxidation gives rise to core–shell nanoparticles, whose surface is terminated by an amorphous mixed Au–In oxide shell surrounding an Au–In alloy core. The oxide is enriched in Au, and its surface layer contains Au embedded in the oxide. Although this is a metastable state, we find that it is stable against phase separation up to high temperatures.

Author contributions: E.A.S. and P.W.S. designed research; E.A.S., X.T., K.J., and P.W.S. performed research; E.A.S. and P.W.S. analyzed data; and E.A.S. and P.W.S. wrote the paper.

The authors declare no conflict of interest.

This article is a PNAS Direct Submission.

[1]To whom correspondence should be addressed. E-mail: esutter@bnl.gov.

Downloaded by guest on April 16, 2021

The Au-rich mixed Au–In oxide is capable of adsorbing both CO and O_2, and shows their reaction to CO_2 near room temperature. This system represents a novel approach toward Au-based oxidation catalysts, which do not rely on any particular support, do not require any complex synthesis processes, and resist deactivation up to at least 300 °C.

Results and Discussion

We have pursued a strategy for improving the stability of Au–O catalysts that is based on dispersing Au in a stable amorphous oxide layer. The synthesis of such catalysts involves the room temperature oxidation in air of bimetallic Au–In nanoparticles, formed by sequential evaporation of In and Au on different supports (SiO_2, amorphous C, Ge; see *Materials and Methods* for details). We have investigated two different compositions of Au–In nanoparticles, synthesized by deposition of 2- and 6-nm In (equivalent thickness), followed by deposition of 2-nm Au, which for all substrates considered here produces alloy nanoparticles. In and Au readily interdiffuse at room temperature and form different intermetallic compounds depending on the Au:In ratio (26, 27). During the evaporation of Au on In, an Au layer is never established but instead a Au–In alloy forms one monolayer at a time (28).

Figs. 1 and 2 show transmission electron microscopy (TEM) analysis of the morphology and composition of ensembles of Au-rich and In-rich Au–In nanoparticles, respectively. The nanoparticles show a wide distribution of sizes, from 2–3 to 20 nm. Electron diffraction patterns (DPs) along with TEM imaging establish the structure of the nanoparticles. The ensemble in Fig. 1*A* gives rise to a polycrystalline-type DP (Fig. 1*B*, left side) because the field of view encompasses several particles with random orientation. The DPs consist of discrete spots on rings that are readily indexed to the orthorhombic Au_3In phase (29) for the sample with high Au content (Fig. 1*B*, right side: calculated DP). The sample with three times higher nominal In coverage consists of nanoparticles with the cubic $AuIn_2$ structure (29) (Fig. 2 *B* and *C*). High-resolution TEM and *Z*-contrast imaging (Figs. 1 *C* and *D*, and 2*D*) show nonuniform contrast, similar to pure In particles exposed to ambient air at room temperature (2). The particles have a core–shell structure, consisting of single crystalline cores and thin amorphous shells,

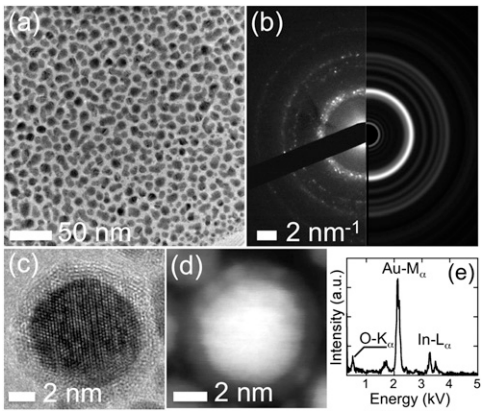

Fig. 1. Structural and compositional analysis of high-Au content Au–In alloy nanoparticles on amorphous carbon films at room temperature. (*A*) Overview TEM image of an array of nanoparticles. (*B*) (*Left*) Electron diffraction pattern measured on the nanoparticle array. (*Right*) Simulated electron diffraction pattern for nanoparticles with the orthorhombic Au_3In structure. (*C* and *D*) High-resolution TEM and *Z*-contrast images of representative nanoparticles from the array, showing their core–shell structure consisting of a crystalline Au_3In core and amorphous oxide shell. (*E*) EDS composition analysis of the nanoparticles.

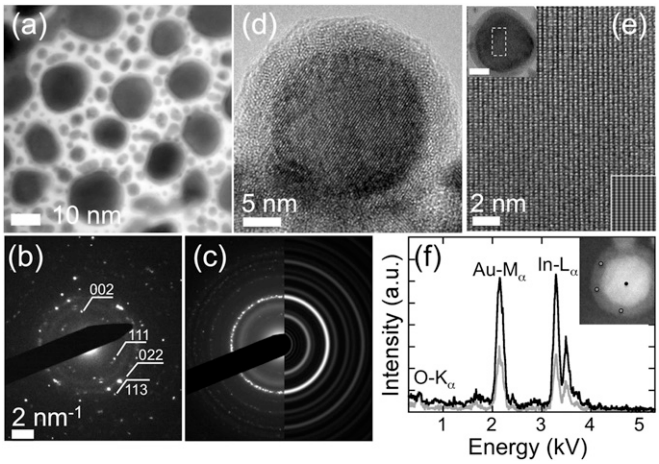

Fig. 2. Structural and compositional analysis of low-Au content Au–In alloy nanoparticles on amorphous carbon films at room temperature. (*A*) Overview TEM image of the nanoparticles. (*B*) Electron diffraction pattern, measured on the nanoparticles in *A*, showing discrete spots indexed with the cubic $AuIn_2$ structure. (*C*) (*Left*) Electron diffraction pattern, measured on a larger nanoparticle array (~6.5 μm^2). (*Right*) Simulated electron diffraction pattern for nanoparticles with the cubic $AuIn_2$ structure. (*D*) High-resolution TEM image of a nanoparticle at the edge of the carbon film, showing the core–shell structure consisting of crystalline $AuIn_2$ core and amorphous oxide shell. (*E*) High-resolution TEM image of the crystalline core of a representative nanoparticle shown in the *Upper Left Inset*. (Scale bar: 10 nm.) *Lower Right Inset* shows the calculated high-resolution TEM image, simulated using the multislice method as implemented in the software package JEMS (48). (*F*) Characteristic EDS spectra from the core and shell of a nanoparticle, whose *Z*-contrast image is shown in *Inset*.

separated by an atomically sharp interface. Energy-dispersive X-ray spectroscopy (EDS) analysis confirms that the cores of the Au-rich nanoparticles contain ~25 atomic (at.) % In and ~75 at. % Au (Fig. 1*E*), close to Au_3In alloy inferred from the DPs, whereas the In-rich nanoparticles (Fig. 2*F*) show Au in the range of 32–35 at. % and 65–68 at. % In. The outer shell is assigned to an oxide, formed by the oxidation of the particles upon room temperature exposure to air. In contrast to the oxidation of In nanoparticles under similar conditions (2, 5), which results in crystalline In_2O_3 shells (2), for Au–In alloy nanoparticles the oxide shells are amorphous, i.e., show no crystalline order. Statistical analysis (for ~50 particles per sample) shows a uniform thickness of the oxide shells of 1.6 ± 0.4 nm for Au_3In and 2.3 ± 0.4 nm for $AuIn_2$ nanoparticles. The thicker oxide of the In-rich particles allows reliable EDS analysis of the shell composition, which shows a Au:In ratio close to the one of the core (Fig. 2*F*). Thus, the oxidation of Au–In alloy nanoparticles in air produces Au–In alloy-oxide core–shell structures, whose oxide shells are amorphous with composition mirroring that of the alloy cores.

The formation of a stable amorphous two-component oxide has important ramifications. If found to be a general process applicable to a wider range of materials, it could open avenues for the preparation of mixed oxide or oxide-embedded noble metal catalysts, beyond the (Au–In)-oxide system discussed here. At first glance, both the lack of phase separation upon oxidation of the Au–In alloy nanoparticles and the formation of an amorphous oxide appear unusual. Indeed, according to the current picture of the oxidation of binary alloys consisting of components A and B with very different affinities toward oxygen, i.e., one (A) noble with respect to oxidation, a single oxide of the less noble component (B) is expected to form (30, 31). Our previous experiments have demonstrated that the oxidation of In nanoparticles (2, 5) proceeds via oxygen penetration through the growing oxide, i.e., the inward diffusion of oxygen anions is faster

Downloaded by guest on April 16, 2021

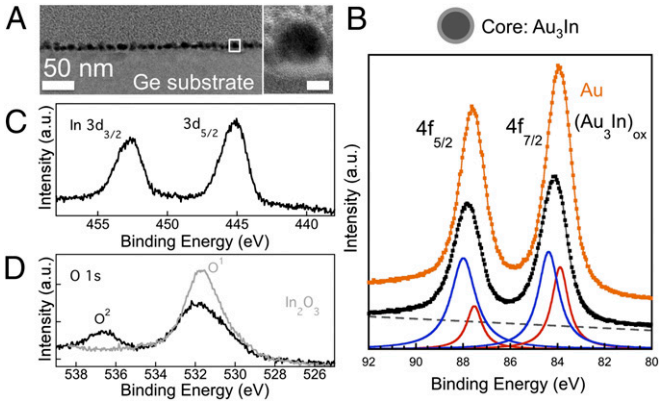

Fig. 3. (*A*) Cross-sectional TEM image of the Au_3In-amorphous oxide core–shell nanoparticles on Ge(111) substrate. (*Inset*) High-resolution TEM image of a nanoparticle. (Scale bar: 5 nm.) (*B*) X-ray photoelectron spectra of Au 4f core levels of the composite Au_3In-amorphous oxide core–shell nanoparticles [black squares, $(Au_3O)_{ox}$] compared with the Au 4f spectra of a high-purity gold standard (orange squares, Au). The experimental XPS spectrum from the Au standard was fitted with single Lorentzians for the $4f_{5/2}$ and $4f_{7/2}$ peaks (orange curve). The fit for the XPS spectra from the Au_3In-oxide core–shell nanoparticles (black curve) involved two Lorentzians for each of the $4f_{5/2}$ and $4f_{7/2}$ peaks (blue and red curves; see text). (*C*) X-ray photoelectron spectrum of In 3d core levels from the composite Au_3In-amorphous oxide core–shell nanoparticles. (*D*) O 1s spectrum from the oxide shell of the composite nanoparticles in *A*, compared with a reference sample of In_2O_3 nanoparticles on Ge substrate.

than the outward diffusion of cations, similar to Pb, Pb–Sn, and Pb–In (6, 32–38). In this case, oxidation occurs at the metal alloy–oxide interface and does not involve the phase separation of the noble component, as shown by previous experiments on the oxidation of Pb–Sn and Au–In bulk alloys (where Pb is the species with lower affinity to oxygen). The example of Pb–In oxidation has shown that the oxide always contains both the noble and less noble metal components, as long as they are fully miscible in the alloy. Only above the solubility limit, phase separation occurs and the In oxidizes to pure In_2O_3. The absence of phase separation also explains the formation of an amorphous oxide. O anion diffusion from the surface is sufficient to produce an oxide with short-range metal–oxygen coordination, but the presence of Au appears to limit the overall mobility of the In atoms/ions so as to preclude the formation of the long-range ordered structure of a crystalline oxide.

We further probed the core–shell nanoparticles using X-ray photoelectron spectroscopy (XPS) to determine the composition and chemical environment, and low-energy ion-scattering spectroscopy (ISS) to identify the elements exposed in the outermost atomic layer. Both investigations were performed on oxidized nanoparticle ensembles on Ge substrates. Fig. 3*A* is an overview cross-sectional TEM image of the (Au_3In)–(amorphous Au–In oxide) core–shell nanoparticles showing a dense ensemble of approximately spherical nanoparticles surrounded by amorphous oxide shells seen as a thin ring of lighter contrast in high-resolution TEM (Fig. 3*A*, *Inset*).

XPS on both Au_3In (Fig. 3 *B–D*) and $AuIn_2$ nanoparticles reveals the presence of Au, In, and O. We focus the further analysis on the Au-rich Au_3In alloy. Here, the Au 4f peaks are broadened and their center shifted to higher binding energy (BE) compared with a Au reference (Fig. 3*B*) (*Discussion*). The In $3d_{5/2}$ peak (~445.15 eV; Fig. 3*C*) is shifted to higher energies by ~1 eV compared with bulk Au_3In alloys whose surface oxide has been removed by sputtering (39). XPS measurements on bulk AuIn with native oxide show a similar shift (~0.7 eV) for the BE of the In $3d_{5/2}$ peak. Thus, it is reasonable to assume that the shifts in In 3d core levels relative to the binding energies of the bulk alloys are due to contributions from both the particle cores (metallic Au–In alloys) and the oxide shells.

Curve fitting of the Au 4f spectrum from the oxidized Au_3In nanoparticles (Fig. 3*B*) shows that the broadened $4f_{5/2}$ and $4f_{7/2}$ lines actually consist of two peaks. The intense peaks at higher BE (88.0 and 84.4 eV, respectively) match those reported for bulk Au_3In alloys (39), which also show very similar intensity ratios. The less intense peaks are shifted by 0.5 eV to lower BE (87.5 and 83.9 eV, respectively), and match the Au 4f peaks of a bulk Au reference sample (Fig. 3*B*, orange squares). From this analysis, we conclude that the first set of peaks originates from the bimetallic Au_3In alloy core of the nanoparticles. The second set can be associated with the mixed-oxide shell, and its close match with the Au reference spectrum suggests the presence of small Au clusters in the mixed Au–In oxide.

Although the Au 4f and In 3d XPS signal (Fig. 3 *B* and *C*) has components from both the core and the shell of the nanoparticles, the oxygen 1s signal should reflect only the composition and binding in the amorphous oxide shell and of possible adsorbed species. Fig. 3*D* compares the O 1s peak of oxidized Au–In nanoparticles with high Au content (Au_3In cores) with a reference measurement on indium oxide (In_2O_3) nanoparticles (gray curve). The O 1s XPS spectrum for the In_2O_3 nanoparticles has a single peak (O^1; Fig. 3*D*) centered at 531.7 eV, in excellent agreement with results on In_2O_3 powders and thin films (40, 41). In the O 1s spectrum of the (Au_3In)–(Au–In oxide) core–shell nanoparticles, two peaks are clearly resolved. The lower-energy peak is identical to the O^1 line of pure In_2O_3, i.e., represents O in the mixed oxide with primarily In_2O_3-like coordination. The higher energy peak, O^2, at ~536.2 eV is unusual as it points to a large chemical shift (more than 5 eV) relative to O^1. Such a high BE would normally be associated with weakly adsorbed or physisorbed surface oxygen species (42). Our XPS measurements were carried out on samples that had been annealed to temperatures (473 K) sufficient to desorb weakly bound species. Thus, the high-energy peak either originates from oxygen coordinated to Au in the oxide shell, or from a strongly bound adsorbate. The fact that this peak is not observed for In_2O_3

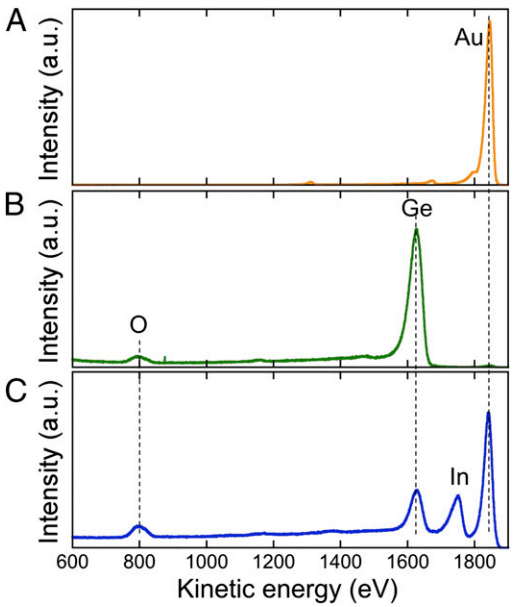

Fig. 4. Ion scattering spectra of the following: (*A*) Reference Au film. (*B*) Reference Ge wafer, used as a substrate for the nanoparticles. (*C*) Au_3In-amorphous Au–In oxide core–shell nanoparticles, as shown in Fig. 3*A*.

Downloaded by guest on April 16, 2021

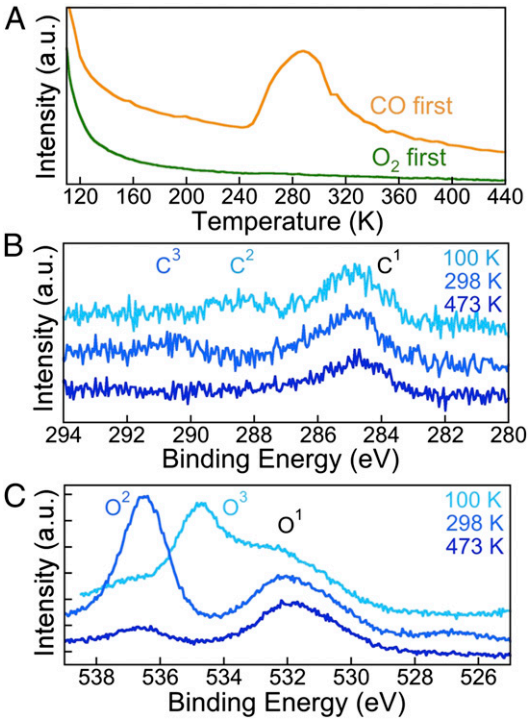

Fig. 5. (*A*) TPD spectra of CO_2 (mass 44) after dosing of Au_3In-amorphous oxide composite nanoparticles with 600 L of CO followed by 600 L of O_2 (orange curve) at 100 K, compared with sequential dose of 600 L of O_2 followed by 600 L of CO (green curve). (*B*) Carbon 1s and (*C*) oxygen 1s XPS spectra of the same sample taken after the exposure to CO followed by O_2 at 100 K, and further heating to 298 and 473 K, respectively.

nanoparticles implies the presence of chemically reactive Au species on the surface of the mixed Au–In oxide. This picture finds support in a recent XPS study on Au oxidation in high-frequency discharges, which showed a similar high-energy O 1s peak after long exposure of Au to oxygen (42, 43).

The surface composition of oxidized Au–In alloy nanoparticles was determined by low-energy ISS (Fig. 4 *A*–*C*). An Au film on Ge (Fig. 4*A*) and bulk Ge (with native oxide; Fig. 4*B*) were used as reference samples. ISS on the Au–In oxide shows the presence of Au, In, Ge, and O on the surface (Fig. 4*C*). The Ge signal likely stems entirely from the exposed support between the nanoparticles. The (Au:In) peak ratios in samples with different In content show that the oxide surface of particles with Au_3In cores contains significantly more Au (Au:In = 2.72) than that of particles with $AuIn_2$ cores (Au:In = 1.22). At the same time, the O:In ratios are nearly the same for both types of samples (Au_3In: 0.44; $AuIn_2$: 0.51). The ISS measurements thus confirm that the outermost atomic layer of the amorphous oxide shell of the nanoparticles contains Au, In, and O, and that its Au content depends on the Au concentration in the initial Au–In binary alloy.

The formation of an amorphous mixed Au–In oxide with exposed Au on the surface from particles of binary alloys that oxidize via predominant anion transport could represent a previously unexplored avenue toward the synthesis of Au-based catalysts. To investigate the activity of such systems in oxidation catalysis, we followed CO oxidation on CO/O_2 covered particles by temperature-programmed desorption (TPD), complemented by XPS. The surface of the particles was dosed at 100 K with O_2 and CO in two different ways: 600 L of CO followed by 600 L of O_2, and 600 L of O_2 followed by 600 L of CO. TPD was performed between 100 and 473 K. Fig. 5*A* shows TPD of CO_2 evolution (mass 44) from the surface of the Au–In oxide particles with Au-rich (Au_3In) cores. When CO was dosed before O_2, a prominent CO_2 desorption peak with maximum intensity around 288 K developed (Fig. 5*A*, orange curve). CO, O, and C signals (masses 28, 16, and 12) evolved in amounts corresponding to the cracking pattern of CO_2. Repeated low-temperature CO dosing, followed by O_2 adsorption and annealing led to the same CO_2 evolution. When O_2 was dosed before CO (Fig. 5*A*, green curve), no peaks were observed in the entire temperature range. Exposure to O_2 at cryogenic temperatures clearly fills adsorption sites on the surface and precludes the adsorption of CO, and in this case no reaction to CO_2 occurs. Finally, reference In_2O_3 particles were not active in CO oxidation.

XPS measurements at three different temperatures on samples exposed to CO, followed by O_2 at 100 K were used to follow the carbon- and oxygen-containing species (Fig. 5 *B* and *C*) during the reaction to CO_2. Following the adsorption, the C 1s spectrum of the nanoparticles shows two peaks: C^1, BE ~285 eV, and a relatively weak C^2, BE ~288.5 eV. C^1 was present after prolonged initial annealing at 473 K, before adsorption of gases, and persists throughout our experiments; it is consistent with the presence of carbon or hydrocarbons on the surface (44, 45). It is reasonable to associate C^2, detected after exposure to CO and O_2 at 100 K, to the presence of CO on the surface. Gas phase CO has a BE ~290 eV (45), but chemisorption of CO on oxides leads to significant (>3 eV) broadening of the peak and shifts in the BE (46), consistent with our observation (Fig. 5*B*). In addition to the In_2O_3-like feature O^1, which is always present, the O 1s XPS spectrum at 100 K shows the formation of a new peak O^3 that can also be associated with adsorbed CO and O_2. Increasing the temperature to 298 K leads to clear changes in both the C 1s and O 1s XPS spectra. C^2 and O^3 disappear, and new peaks C^3 (BE, ~290.6 eV) and O^2 dominate the spectra. Two things point in favor of C^3 being associated with CO_2: (*i*) The C 1s BE of CO_2

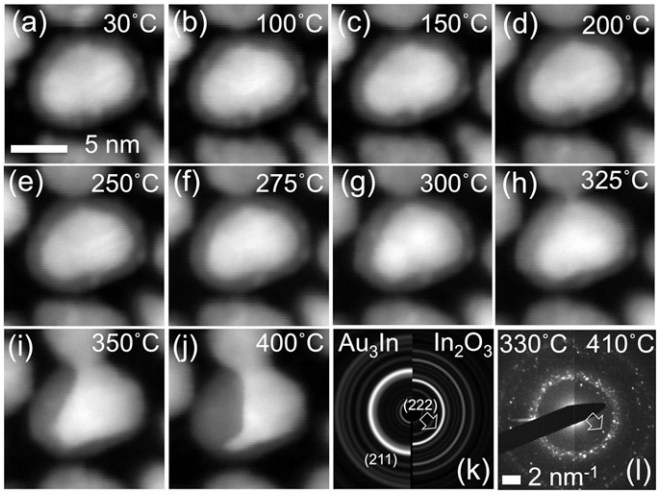

Fig. 6. Thermal stability of mixed-oxide terminated Au–In alloy nanoparticles. (*A*–*J*) Sequence of *Z*-contrast STEM images showing a characteristic nanoparticle with Au_3In core and amorphous oxide shell from an ensemble similar to that of Fig. 1*A* during in situ annealing up to 400 °C. (*K*) Comparison of the calculated electron diffraction patterns of Au_3In and In_2O_3. (*L*) Measured electron diffraction patterns from the entire nanoparticle ensemble at 330 °C (*Left*) and 410 °C (*Right*). The experimental diffraction pattern at 330 °C is identical to the one at room temperature (Fig. 1*B*), indexed to the Au_3In structure. The diffraction pattern at 410 °C contains a ring of additional spots (arrow) that appear upon annealing above 350 °C, where the amorphous oxide shell begins to crystallize. The arrow in *K* marks the corresponding ring in the calculated diffraction pattern, which stems from the (222) lattice planes of In_2O_3.

Downloaded by guest on April 16, 2021

should be shifted to higher energies compared with CO (45). (*ii*) C^3 appears at a temperature, where TPD shows CO_2 desorption. A further temperature increase to 473 K eliminates C^3 and significantly lowers the intensity of O^2, so that both the C 1s and O 1s XPS spectra are reverted to their initial state.

The finding that mixed Au–In oxide terminated nanoparticles remain active in catalyzing CO oxidation even after annealing to 200 °C suggests a stability of the active phase that is unusual for a Au-based material. To evaluate the stability of the amorphous Au–In oxide, we followed an ensemble of nanoparticles during heating in vacuum (up to 700 °C) and during exposure to hydrogen, both in situ in the TEM. The amorphous oxide was not reduced and remained unchanged during exposure to 1 torr H_2 at temperatures below 300 °C, conditions under which other metal oxides (e.g., NiO) are found to be reduced readily. A representative sequence of *Z*-contrast images of one particle during vacuum annealing is shown in Fig. 6. Up to 300 °C, the particle does not change (Fig. 6 *A*–*H*). Above 300 °C, both the core and the oxide shell show first signs of restructuring. Around ~350 °C, the oxide shell changes drastically (Fig. 6*I*) as it opens and migrates to one side of the particle. TEM imaging together with diffraction of large ensembles (Fig. 6 *K* and *L*) shows that the restructuring is accompanied by crystallization of the oxide into the c-In_2O_3 structure. As the Au_3In cores are no more completely encapsulated in oxide shells but are merely attached to the now crystalline In_2O_3, the metal alloy segments of neighboring particles start coalescing. Crystallization of the oxide shell was observed at lower temperatures in the nanoparticles with $AuIn_2$ cores, for which already at 300 °C the majority of the particles had crystalline In_2O_3 partial shells.

Conclusions

In summary, the room temperature oxidation of Au–In alloy nanoparticles with different Au content results in the formation of particles in which a metallic Au–In alloy core is encapsulated in a mixed Au–In oxide. The mixed oxide is amorphous in contrast to the polycrystalline In_2O_3 formed in oxidation of In nanoparticles. Au is present in the oxide, including its outermost layer, in amounts determined by the composition of the Au–In alloy. The oxidation of the binary alloy appears to be the only route toward such mixed oxides. For instance, Au does not react with In_2O_3 even at elevated temperatures (47). The mixed oxide shows excellent stability during annealing to elevated temperatures, and it is active in catalyzing the reaction of CO and O_2 to CO_2. Our combined results suggest room temperature oxidation of binary alloys that oxidize via predominant anion transport as a simple process for the preparation of stable Au-based nanocatalysts. A key remaining question is the identification of the catalytically active sites in such materials. Here, the comparison of Au- and In-rich samples provides some guidance. TEM (Fig. 1*B*) and high-angle annular dark-field (HAADF) scanning TEM (STEM) (Figs. 1*C* and 6) on nanoparticles with Au-rich mixed oxides surrounding Au_3In cores, which we find to be particularly active, shows small (~1 nm) clusters anchored in the surface of the amorphous oxide shell. These clusters have higher atomic number (*Z*) than the surrounding oxide, i.e., are Au (or at least Au-rich) particles. The presence of such Au-rich clusters in the mixed oxide is supported by our XPS analysis of oxidized Au_3In nanoparticles (Fig. 3*B*). In contrast, the mixed-oxide shells of In-rich ($AuIn_2$) nanoparticles are featureless and do not show embedded particles (Fig. 2 *A* and *B*). Hence, the active sites in our materials can be Au atoms or small Au clusters. Their embedding in an amorphous Au–In oxide matrix appears to be the key to their high thermal stability.

Materials and Methods

Bimetallic Au–In alloy nanoparticles were formed by sequential room temperature evaporation of controlled amounts of In and Au on SiO_2 and amorphous carbon membranes supported on standard TEM grids as well as Ge(111) substrates. Pure In nanoparticles for control experiments were formed by evaporation of In under identical conditions. The as-deposited nanoparticle ensembles were exposed to ambient conditions after removal from the growth reactor, which led to their oxidation in air. The morphology and composition of the nanoparticles were investigated by TEM in a JEOL 2100F field emission microscope equipped with a Gatan HAADF detector for incoherent HAADF or *Z*-contrast imaging in STEM mode, and for EDS in scanning TEM mode (beam size, 0.2 nm). Variable-temperature (room temperature to 700 °C) TEM experiments were carried out using a Gatan-652 sample holder. XPS, low-energy ISS, and TPD measurements were carried out after extensive (several hours) annealing at 200 °C in a ultrahigh-vacuum system with 1–3 $\times$ 10^{-10} torr base pressure, equipped with a SPECS Phoibos 100 spectrometer and a quadrupole mass spectrometer (Pfeiffer Prisma Plus QMG 220 M2) with entrance aperture in proximity (~2 mm) of the sample. The composition was probed by XPS using Al K_α radiation ($\eta\nu$ = 1,486.61 eV) on nanoparticle ensembles deposited on Ge(111) substrates. The Ge $2p_{3/2}$ spectral line of the substrate served as energy reference in all spectra. The surface composition was probed by ISS measurements using 2-keV He ions (SPECS IQE 12/38 ion source). The activity in oxidation catalysis was studied by TPD after adsorption of different amounts of CO and oxygen on the surface at 100 K. The TPD was done at a heating rate of 0.5 K/s. In each run, the CO, O_2, H_2O, CO_2, and C masses were followed.

ACKNOWLEDGMENTS. We thank Kim Kisslinger for technical assistance. This work was performed at the Center for Functional Nanomaterials, Brookhaven National Laboratory, under the auspices of the Department of Energy, under Contract DE-AC02-98CH10886.

1. Cabrera N, Mott NF (1948) Theory of the oxidation of metals. *Rep Prog Phys* 12(1): 163–184.
2. Sutter E, Sutter P (2012) Size-dependent room temperature oxidation of in nanoparticles. *J Phys Chem C* 116(38):20574–20578.
3. Ermoline A, Dreizin EL (2011) Equations for the Cabrera-Mott kinetics of oxidation for spherical nanoparticles. *Chem Phys Lett* 505(1–3):47–50.
4. Zhdanov VP, Kasemo B (2008) Cabrera-Mott kinetics of oxidation of nm-sized metal particles. *Chem Phys Lett* 452(4–6):285–288.
5. Sutter E, Sutter P (2012) Enhanced oxidation of nanoscale in particles at the interface with a Si nanowire. *Appl Phys Lett* 100(23):231602–231606.
6. Nakamura R, Tokozakura D, Nakajima H, Lee JG, Mori H (2007) Hollow oxide formation by oxidation of Al and Cu nanoparticles. *J Appl Phys* 101(7):074303–074307.
7. Yin YD, et al. (2004) Formation of hollow nanocrystals through the nanoscale Kirkendall effect. *Science* 304(5671):711–714.
8. Cabot A, et al. (2007) Vacancy coalescence during oxidation of iron nanoparticles. *J Am Chem Soc* 129(34):10358–10360.
9. Nakamura R, Lee JG, Mori H, Nakajima H (2008) Oxidation behaviour of Ni nanoparticles and formation process of hollow NiO. *Philos Mag* 88(2):257–264.
10. Schaak RE, et al. (2005) Metallurgy in a beaker: Nanoparticle toolkit for the rapid low-temperature solution synthesis of functional multimetallic solid-state materials. *J Am Chem Soc* 127(10):3506–3515.
11. Klobukowski ER, Angelici RJ, Woo LK (2012) Bulk gold-catalyzed oxidations of amines and benzyl alcohol using amine N-oxides as oxidants. *Catal Lett* 142(2):161–167.
12. Klobukowski ER, Angelici RJ, Woo LK (2012) Bulk gold-catalyzed reactions of isocyanides, amines, and amine N-oxides. *Organometallics* 31(7):2785–2792.
13. Haruta M (1997) Size- and support-dependency in the catalysis of gold. *Catal Today* 36(1):153–166.
14. Janssens TVW, et al. (2007) Insights into the reactivity of supported Au nanoparticles: Combining theory and experiments. *Top Catal* 44(1–2):15–26.
15. Gajan D, et al. (2009) Gold nanoparticles supported on passivated silica: Access to an efficient aerobic epoxidation catalyst and the intrinsic oxidation activity of gold. *J Am Chem Soc* 131(41):14667–14669.
16. Min BK, Alemozafar AR, Pinnaduwage D, Deng X, Friend CM (2006) Efficient CO oxidation at low temperature on Au(111). *J Phys Chem B* 110(40):19833–19838.
17. Min BK, Friend CM (2007) Heterogeneous gold-based catalysis for green chemistry: Low-temperature CO oxidation and propene oxidation. *Chem Rev* 107(6):2709–2724.
18. Koeppel RA, Baiker A, Schild C, Wokaun A (1991) Carbon dioxide hydrogenation over Au/ZrO_2 catalysts from amorphous precursors: catalytic reaction mechanism. *J Chem Soc Faraday Trans* 87(17):2821–2828.
19. Zhou SH, et al. (2008) In situ phase separation of NiAu alloy nanoparticles for preparing highly active Au/NiO CO oxidation catalysts. *ChemPhysChem* 9(17): 2475–2479.
20. Zhou SH, et al. (2009) Low-temperature solution-phase synthesis of NiAu alloy nanoparticles via butyllithium reduction: Influences of synthesis details and application as the precursor to active Au-NiO/SiO_2 catalysts through proper pretreatment. *J Phys Chem C* 113(14):5758–5765.

Downloaded by guest on April 16, 2021

21. Bauer JC, et al. (2012) Silica-supported Au-CuOx hybrid nanocrystals as active and selective catalysts for the formation of acetaldehyde from the oxidation of ethanol. *ACS Catal* 2(12):2537–2546.
22. Bauer JC, et al. (2011) Synthesis of silica supported AuCu nanoparticle catalysts and the effects of pretreatment conditions for the CO oxidation reaction. *Phys Chem Chem Phys* 13(7):2571–2581.
23. Liu XY, et al. (2011) Structural changes of Au-Cu bimetallic catalysts in CO oxidation: In situ XRD, EPR, XANES, and FT-IR characterizations. *J Catal* 278(2):288–296.
24. Yu K, Wu Z, Zhao Q, Li B, Xie Y (2008) High-temperature-stable Au@SnO2 core/shell supported catalyst for CO oxidation. *J Phys Chem C* 112(7):2244–2247.
25. Bracey CL, Ellis PR, Hutchings GJ (2009) Application of copper-gold alloys in catalysis: Current status and future perspectives. *Chem Soc Rev* 38(8):2231–2243.
26. Simic V, Marinkovic Z (1977) Thin-film interdiffusion of Au and in at room-temperature. *Thin Solid Films* 41(1):57–61.
27. Bjontegaard J, Buene L, Finstad T, Lonsjo O, Olsen T (1983) Low temperature interdiffusion in Au/In thin film couples. *Metallurgical and Protective Coatings* 101(3): 253–262.
28. Robinson MC, Slavin AJ (1996) Indium adsorption on the Au(111) surface at room temperature. *Phys Rev B Condens Matter* 54(19):14087–14092.
29. Burkhardt W, Schubert K (1959) Uber Messingartige Phasen Mit A3-Verwandter Struktur. *Z Metallk* 50(8):442–452.
30. Wagner C (1956) Oxidation of alloys involving noble metals. *J Electrochem Soc* 103(10):571–580.
31. Zhang MX, Chang YA (1993) Stability of an alloy oxide interface with oxygen ions being the dominant diffusing species in the oxide scale. *Acta Metall Mater* 41(3): 739–746.
32. Thompson BA, Strong RL (1963) Self-diffusion of oxygen in lead oxide. *J Phys Chem* 67(3):594–597.
33. Konetzki RA, Chang YA, Marcotte VC (1989) Oxidation-kinetics of Pb-Sn alloys. *J Mater Res* 4(6):1421–1426.
34. Zhang MX, Chang YA, Marcotte VC (1990) Oxidation-kinetics of a Pb-3 atom percent in alloy. *J Electrochem Soc* 137(10):3158–3162.
35. Zhang MX, Chang YA, Marcotte VC (1990) Oxidation of single-phase Pb-In alloys. *Oxid Met* 33(3–4):301–308.
36. Zhang MX, Chang YA, Marcotte VC (1991) Oxidation-kinetics of a Pb-64 atmospheric-percent in single-phase alloy. *Oxid Met* 36(5–6):465–474.
37. Zhang MX, Chang YA, Marcotte VC (1991) Oxidation of lead-indium single-phase alloys at low-pressures. *Z Metallk* 82(8):599–602.
38. Zhang MX, Chang YA, Marcotte VC (1991) Oxidation-kinetics of a Pb-30 at Pct in alloy. *Metall Trans A* 22(8):1865–1869.
39. Jayne DT, Fatemi NS, Weizer VG (1991) An X-ray photoelectron-spectroscopy study of auxiny alloys. *J Vac Sci Technol A* 9(3):1410–1415.
40. Lin AWC, Armstrong NR, Kuwana T (1977) X-ray photoelectron auger electron spectroscopic studies of tin and indium metal foils and oxides. *Anal Chem* 49(8): 1228–1235.
41. Fan JCC, Goodenough JB (1977) X-ray photoemission spectroscopy studies of Sn-doped indium-oxide films. *J Appl Phys* 48(8):3524–3531.
42. Stadnichenko AI, Koshcheev SV, Boronin AI (2007) Oxidation of the polycrystaline gold foil surface and XPS study of oxygen states in oxide layers. *Moscow Univ Chem Bull* 62(6):343–349.
43. Pireaux JJ, Liehr M, Thiry PA, Delrue JP, Caudano R (1984) Electron spectroscopic characterization of oxygen-adsorption on gold surfaces. 2. Production of gold oxide in oxygen DC reactive sputtering. *Surf Sci* 141(1):221–232.
44. Bachman BJ, Vasile MJ (1989) Ion-bombardment of polyimide films. *J Vac Sci Technol A* 7(4):2709–2716.
45. Gelius U, et al. (1970) Molecular spectroscopy by means of ESCA III. Carbon compounds. *Phys Scr* 2(1–2):70–80.
46. Freund HJ, et al. (1993) Adsorption and reaction of molecules on surfaces of metal-metal oxide systems. *J Mol Catal* 82(2–3):143–169.
47. Goral JP, Eyring L (1986) The gold indium thin-film system—a high-resolution electron-microscopy study. *J Less Common Met* 116(1):63–72.
48. Stadelmann P (2012) jems, ems java version. Available at http://cimewww.epfl.ch/people/stadelmann/jemsWebSite/jems.html. Accessed March 20, 2013.

Downloaded by guest on April 16, 2021